NANO LETTERS

pubs.acs.org/NanoLett Letter

High-Mobility Carriers in Epitaxial IrO_2 Films Grown using Hybrid Molecular Beam Epitaxy

Sreejith Nair,* Zhifei Yang, Kevin Storr, and Bharat Jalan*

Cite This: *Nano Lett.* 2024, 24, 10850−10857 Read Online

ACCESS | Metrics & More | Article Recommendations | Supporting Information

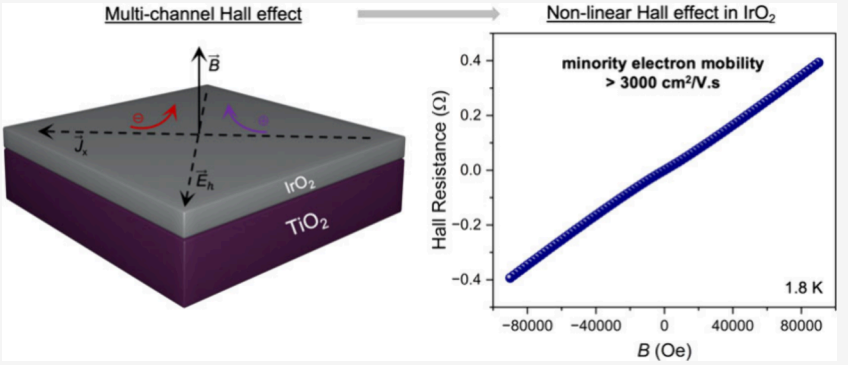

ABSTRACT: Binary rutile oxides of 5d metals such as IrO_2 stand out in comparison to their 3d and 4d counterparts due to limited experimental studies, despite rich predicted quantum phenomena. Here, we investigate the electrical transport properties of IrO_2 by engineering epitaxial thin films grown using hybrid molecular beam epitaxy. Our findings reveal phonon-limited carrier transport and thickness-dependent anisotropic in-plane resistance in IrO_2 (110) films, the latter suggesting a complex relationship between strain relaxation and orbital hybridization. Magnetotransport measurements reveal a previously unobserved nonlinear Hall effect. A two-carrier analysis of this effect shows the presence of minority carriers with mobility exceeding 3000 $cm^2/(V\ s)$ at 1.8 K. These results point toward emergent properties in 5d metal oxides that can be controlled using dimensionality and epitaxial strain.

KEYWORDS: *nonlinear Hall effect, anisotropic transport, strain relaxation, hybrid molecular beam epitaxy*

The rutile crystal structure has emerged over the years as a host of exotic quantum effects with the discovery of unconventional properties in materials like VO_2 and RuO_2. 3d VO_2 has now been studied for decades due to its near-room-temperature coupled structural and metal−insulator transition[1,2] for use in smart windows,[3] field effect Mott transistors,[4] and neuromorphic computing.[5] 4d RuO_2, on the other hand, has come to the forefront more recently with the discovery of strain-induced superconductivity,[6] nontrivial band topology,[7] altermagnetism[8−11]—a novel magnetic state, and associated spintronic functionalities.[12−14] However, the 5d counterpart IrO_2, although of great technological interest, has received relatively less attention.

The interest in IrO_2,[15] and the iridate family in general, has multiple origins and motivations. Numerous predictions of nontrivial topology,[16,17] quantum criticality,[18] and unconventional superconductivity[19] have surrounded the iridium oxides. One of the key examples, for instance, has been the prediction and experimental observation of topological line nodes[20,21] and large Berry curvature induced spin-Hall conductivity in perovskite $SrIrO_3$.[22] Such large spin-Hall conductivities can significantly improve device performance, with the perovskite structure allowing further integration with many other material systems. However, from a commercial standpoint, binary oxides may be preferred due to their ease of synthesis and reproducibility. With growing literature on perovskite-like quantum properties in simple binary oxides, they can form a comprehensive, efficient, and scalable quantum system.

Like the perovskite $SrIrO_3$, rutile IrO_2 has been shown to have Dirac nodal lines (DNLs) close to the Fermi level using density functional theory[23] (DFT) and angle-resolved photoemission spectroscopy (ARPES) measurements.[24−26] High spin-Hall conductivity arising due to these DNLs[27,28] has also been reported, in line with theoretical predictions.[23] Significant work has also been done to confirm the presence of the predicted $J_{eff} = 1/2$ states[29−31] using spectroscopic techniques, although the debate remains unsettled. In contrast to the numerous spectroscopic characterizations, only a few stud-

Received: May 19, 2024
Revised: August 12, 2024
Accepted: August 14, 2024
Published: August 22, 2024

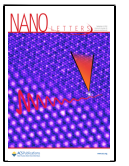

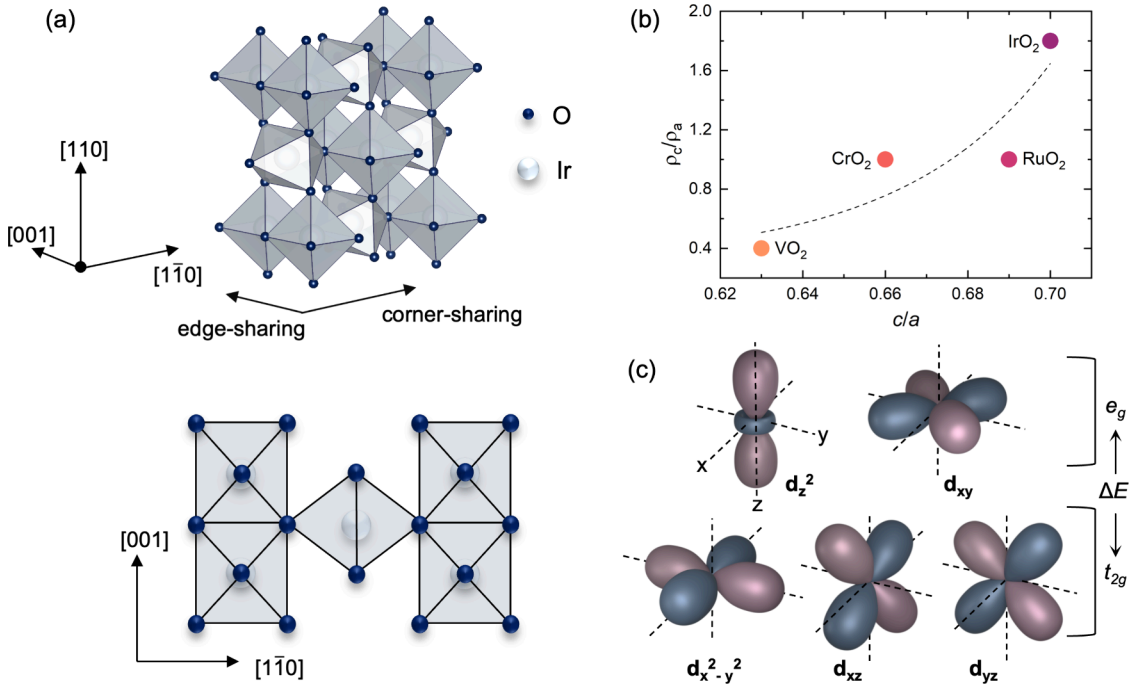

Figure 1. (a) (top) Rutile IrO_2 crystal structure with modified unit cell for thin film grown along the [110] out-of-plane direction. (bottom) 2D projection of the crystal along [110] for better visualization of the edge-shared and corner-shared octahedral network along the [001] and [1$\bar{1}$0] crystal directions. (b) Reported electrical resistivity anisotropy between the rutile *c* and *a* axes for bulk single crystals of metallic rutile VO_2[52] (reproduced with permission from ref 52, copyright Elsevier 1965), CrO_2[53] (reproduced with permission from ref 53, copyright The Physical Society of Japan 1966), and RuO_2[38] and IrO_2[38] (reproduced with permission from ref 38, copyright Elsevier 1968). The dashed line is a trend line. (c) Schematic of the d-orbital shapes and rutile crystal field splitting (ΔE) into lower energy t_{2g} and higher energy e_g manifolds. The *x*, *y*, and *z* axes are consistent for all orbitals and defined along the [001], [1$\bar{1}$0], and [110] directions, respectively, for the edge-shared octahedra.

ies[32−34] have reported the normal state electronic transport in rutile IrO_2, particularly in epitaxial thin films.

The rutile crystal structure (hereafter described using the tetragonal $a = b$ and c axes) inherently lends many intriguing aspects to the electronic structure. The mixed edge and corner-shared anion octahedra as shown in Figure 1a is a key ingredient for most unconventional properties in rutile systems[35] with the metal−metal dimerization along the *c*-axis in VO_2 being a prime example. Further, the low-symmetry (D_{2h}) distorted-octahedral ligand field creates a nondegenerate t_{2g} band with the d orbital parallel (denoted $t_{\parallel}$ in the Goodenough notation[36]) to the *c*-axis ($d_{x^2-y^2}$ orbital in Figure 1c) having minimal hybridization with O 2p orbitals and density of states at the Fermi level.[29,30,37]

With this context of topology and orbital character of the Fermi surface, we analyzed the electronic transport in epitaxial IrO_2 thin films measured as a function of temperature, magnetic field, dimensionality, strain, and epitaxial orientation. The temperature-dependent resistivity from 300 to 1.8 K revealed phonon-dominated carrier scattering with resistivity-temperature exponent $n > 1$, consistent with a Debye temperature higher than 300 K, extracted from a Bloch−Grüneisen type model. Further, in agreement with bulk IrO_2,[38] the resistance along the rutile *c*-axis was found to be greater than that along the perpendicular direction. This anisotropy was also found to be thickness-dependent, suggesting an epitaxial strain effect on the Ir 5d−O 2p hybridization. Hall effect measurements showed a nonlinear dependence of Hall resistance on magnetic field. A two-carrier analysis revealed the presence of high-mobility minority carriers. The validity of the two-carrier model was further confirmed with the observation of electron- or hole-dominated conduction in IrO_2 films with varying epitaxial orientations. This emergence of previously unobserved high-mobility carriers in IrO_2 opens new questions and avenues for engineering quantum phases in iridium-based oxides by tuning the interplay of strain, dimensionality, and electronic structure.

Molecular beam epitaxy (MBE) has enabled high-structural-quality IrO_2 thin films compared to other approaches.[15] However, MBE of iridium-based oxides is challenging due to the low vapor pressure and oxidation potential of pure iridium. Use of solid metal−organic sources instead has been shown to resolve this bottleneck and produce high-quality metal-oxide thin films.[39−41] With this hybrid MBE approach, we grew single-crystalline, epitaxial IrO_2 films with varying thicknesses and orientations on TiO_2 substrates. The details of growth conditions, sample characterization, and strain relaxation can be found elsewhere[41] and are briefly described in the Methods section of the Supporting Information. Figure 2a shows the temperature-dependent resistivity of IrO_2 (110) films for $2.5 \leq t \leq 21$ nm measured in the van der Pauw configuration. The in-plane resistance anisotropy, defined as the ratio of resistance along the [001] and [1$\bar{1}$0] directions, i.e. $R_{[001]}/R_{[1\bar{1}0]}$ at 300 K, is shown as a function of film thickness in the inset of Figure 2a. The resistance anisotropy ranges between 2 and 5 with a nonmonotonic behavior with increasing thickness.

We first discuss the temperature-dependent resistivity, followed by the resistance anisotropy. As shown in Figure 2a, metallic behavior was observed in films with thicknesses as low as 2.5 nm. A clear upturn in resistivity was observed around 50 K for the 2.5 nm film, suggesting a localization-induced upturn. Such a resistance upturn with decreasing thickness has been

https://doi.org/10.1021/acs.nanolett.4c02367
Nano Lett. 2024, 24, 10850−10857

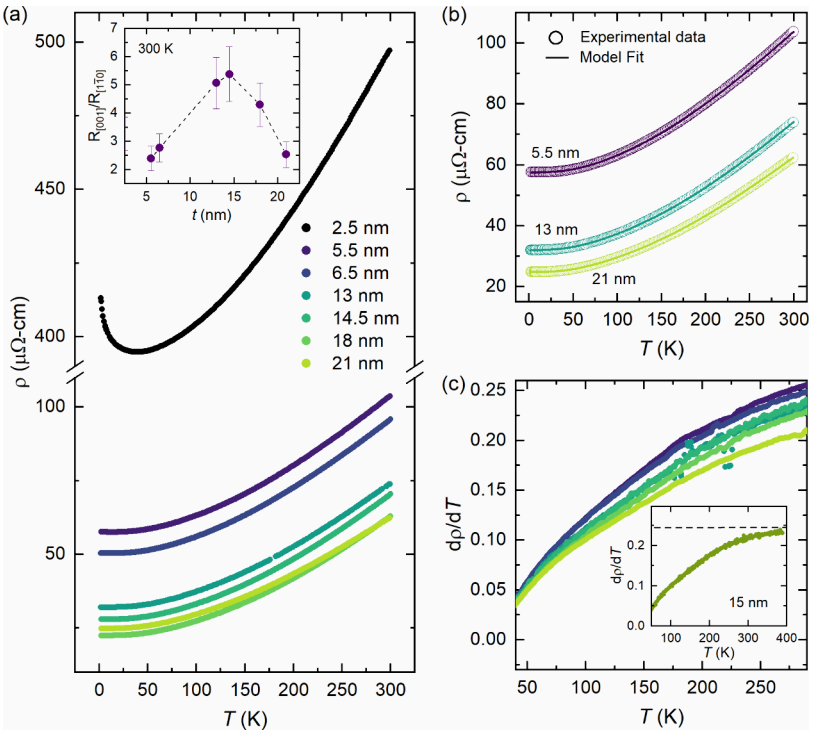

Figure 2. (a) Resistivity as a function of temperature for different thicknesses of IrO_2 (110) films grown on TiO_2 (110) substrate. (inset) Anisotropy in the measured resistance along the in-plane [001] and [1$\bar{1}$0] crystal directions plotted as a function of film thickness. Error bars are calculated using an arbitrary estimate of 12.5% error in the distance between the wire-bonded contact points. (b) Measured resistivity (open circles) and model fit to eq 1 (solid lines) for 5.5, 13, and 21 nm IrO_2 (110) films shown in (a). (c) First-order temperature derivative of resistivity plotted as a function of temperature for the IrO_2 (110) films shown in (a). (inset) First-order temperature derivative of resistivity plotted as a function of temperature for a representative sample measured up to 390 K showing an approach to T-linear behavior indicated by the black dashed line.

observed in many systems,[42−44] including IrO_2,[32] and the mechanisms have been well documented. However, to understand the different scattering contributions to the resistivity, we analyzed our T-dependent resistivity data using a Bloch−Grüneisen type model (see the Supporting Information for more details). Equation 1, which is a combination of the residual resistivity (ρ_o), resistivity due to electron−electron scattering (ρ_{ee}) and acoustic ($\rho_{e\text{-}ph,ac}$) and optical ($\rho_{e\text{-}ph,op}$) phonon scattering, was used to fit the temperature-dependent resistivity.

$$\begin{aligned}\rho(T) &= \rho_o + \rho_{ee}(T) + \rho_{e\text{-}ph,ac}(T) + \rho_{e\text{-}ph,op}(T)\\ &= \rho_o + A_{ee}T^2 + \beta_{ac}T\left(\frac{T}{\theta_D}\right)^2 \int_0^{\theta_D/T} \frac{x^3}{(e^x-1)(1-e^{-x})}\,dx\\ &\quad + \beta_{op}T\left[\frac{\theta_E/2T}{\sinh(\theta_E/2T)}\right]^2 \end{aligned} \quad (1)$$

A_{ee} is the prefactor for the electron−electron scattering term, β_{ac} and β_{op} are measures of the electron−phonon coupling strength for the acoustic and optical branches, and θ_D and θ_E represent the Debye temperature and the temperature corresponding to the Einstein frequency of the optical phonon spectrum, respectively.

Figure 2b shows excellent fits to the experimental data using eq 1 with ρ_o, A_{ee}, β_{ac}, β_{op}, θ_D, and θ_E as the fit parameters. For brevity, only a few thicknesses are shown, and 2.5 nm was excluded from these analyses due to the low-temperature resistance upturn. The extracted fit parameters for the different film thicknesses are tabulated in Table S1. The extracted constants for the electron−phonon coupling contributions are close to those in previous reports.[45,46] Their ratio (β_{ac}/β_{op}) is also in agreement with the calculated values for the closely related rutile RuO_2 (~2) by Glassford and Chelikowsky.[47] The electron−electron scattering term, although included here for better fits at temperatures less than 50−60 K, can be neglected without significant differences in the extracted fit parameters and regression coefficient for the overall fit, as shown in Table S2. The Debye temperature in both cases is around 430−460 K, which is higher than that reported by Lin et al.,[45] but much lower than the value obtained by Ryden et al.[38] Nevertheless, the extracted Debye temperature can be verified based on the expectation of linear T-dependence of resistivity above the Debye temperature for normal metals. Or in other words, the first-order derivative of resistivity with respect to temperature should approach a constant value with increasing temperature above θ_D (430−460 K). To this end, we show in Figure 2c the first-order derivative of resistivity ($d\rho/dT$) as a function of T between 50 and 300 K. The inset shows $d\rho/dT$ vs T for a representative 15 nm IrO_2/TiO_2 (110) up to 390 K. This result shows a nearly constant $d\rho/dT$ value as T increases, which is reasonably consistent with our extracted values of θ_D. The extracted Einstein frequency of ~655 cm^{-1} (corresponding to an average θ_E of ~943 K), however, does not agree with the reported Raman modes for IrO_2[48,49] and the origin of this discrepancy is currently not understood.

https://doi.org/10.1021/acs.nanolett.4c02367
Nano Lett. 2024, 24, 10850−10857

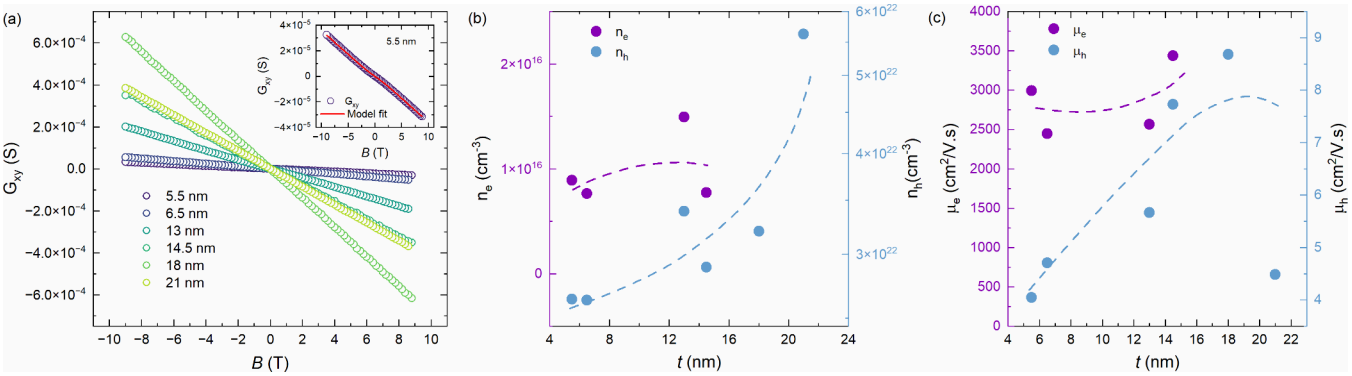

Figure 3. (a) Hall conductance as a function of magnetic field at 1.8 K for different thicknesses of IrO_2 (110) films grown on TiO_2 (110) substrates. (inset) Hall conductance as a function of magnetic field for a 5.5 nm IrO_2 (110) film for better visualization of the nonlinear Hall effect along with a two-carrier model fit. Extracted (b) carrier concentrations and (c) mobilities for the electron and hole channels from two-carrier model fits plotted as a function of film thickness. Dashed lines are guidelines. Straight-line fits were used for 18 and 21 nm films due to vanishing nonlinearity and, hence, solely hole conduction.

It is important to note here that the resistivity analysis was performed on an averaged resistivity[50] obtained using the van der Pauw equation. The measured resistances along the two orthogonal in-plane crystallographic directions are anisotropic, however, as also observed in bulk single crystals where the ratio of resistivity along the *c* and *a* axes (ρ_c/ρ_a) is ∼1.8.[38] As shown in the inset of Figure 2a, the anisotropy ($R_{[001]}/R_{[1\bar{1}0]}$) ranges between 2 and 5 in our IrO_2 thin films, initially increasing and then decreasing as *t* increases. This raises questions about the origin of anisotropy and why it depends on the film thickness. We attribute the former to the anisotropic crystal structure along the [001] and [1$\bar{1}$0] directions and the latter to the strain relaxation in epitaxial IrO_2 (110) films. We attempt to explain the origin of anisotropy qualitatively by referring to the schematics in Figure 1a,c. As described briefly in the introduction, the rutile structure has a network of edge-shared octahedra along the *c*-axis and corner-shared octahedra along the [1$\bar{1}$0] direction. This arrangement is expected to yield contributions to the electrical conduction from the metal−oxygen (M d−O p) orbital hybridization along the M−O−M network and direct M−M hopping along the *c*-axis, whereas the contribution is only from the M−O−M network along the [1$\bar{1}$0] direction. This effect of crystal anisotropy and the relative M−M and M−O−M transport contributions to the resistivity anisotropy at a cursory glance seems to be captured by the tetragonality (c/a) of the rutile crystal. As shown in Figure 1b, there appears to be some correlation between the reported resistivity ratio (ρ_c/ρ_a) and the c/a lattice parameter ratio in bulk metallic rutile oxides.

However, when it comes to the thickness dependence of anisotropy, there is an additional effect of epitaxial strain relaxation. Epitaxial IrO_2 on a TiO_2 (110) substrate experiences a large anisotropic strain with a −6.3% compressive strain along the [001] direction and a +2.3% tensile strain along the [1$\bar{1}$0] direction. So, for a coherently strained film, c/a and, hence, the resistivity anisotropy would be expected to be lowest and eventually increase toward the bulk value with increasing thickness and associated strain relaxation. This expectation, however, contrasts with the observed nonmonotonic variation in anisotropy with thickness shown in the inset of Figure 2a. This necessitates a detailed consideration of the intricacies of the anisotropic-strain-induced octahedral distortion and relative transport contributions from the M−M and M−O−M channels.

For the case of IrO_2, since the $t_{||}$ orbital ($d_{x^2-y^2}$ orbital in Figure 1c, which governs the Ir−Ir interaction along the *c*-axis) has been shown to have negligible density of states at the Fermi level,[29,30] one would expect minimal transport contribution from direct Ir−Ir hopping, assuming the absence of a strain-induced shift of the $t_{||}$ density of states toward the Fermi level. So, the anisotropy in resistance should largely depend on the Ir−O−Ir network along the two in-plane directions, with larger bond angles favoring Ir 5d−O 2p hybridization and, hence, decreased resistance. For a relaxed bulk-like IrO_2 film, the bond angle is higher along [1$\bar{1}$0] (∼128°) as compared to the [001] direction (∼103°) and, hence, $R_{[1\bar{1}0]}$ can be lower than $R_{[001]}$. However, this difference in bond angles and resulting resistance anisotropy can be amplified by the anisotropic strain in IrO_2 (110) film grown on the TiO_2 (110) substrate. The compressive strain along [001] (−6.3%) will push the Ir−O−Ir angle to smaller values (diminishing d−p hybridization) whereas the tensile strain along [1$\bar{1}$0] (+2.3%) will drive the Ir−O−Ir angle to larger values closer to 180° (enhancing d−p hybridization). This change in bond angles, however, is also accompanied by a change in the bond lengths. The compressive strain along [001] will decrease the Ir−O bond length (enhancing d−p hybridization) whereas the tensile strain along [1$\bar{1}$0] will increase the bond length (diminishing d−p hybridization). From this simplified picture of thickness-driven strain relaxation and changes in the Ir−O bond network, the evolution of bond angles toward bulk values with increasing thickness should result in a monotonic *decrease* in the anisotropy ($R_{[001]}/R_{[1\bar{1}0]}$), whereas the simultaneous change in bond lengths should lead to a monotonic *increase* in the anisotropy. Thus, the variation in bond lengths and bond angles as a function of thickness and strain relaxation may act as competing effects and their interplay could lead to the observed nonmonotonic variation of resistance anisotropy. A more careful quantitative study of crystal defects, octahedral distortions, orbital hybridizations, and resulting carrier hopping integrals as a function of strain relaxation is required, however, to accurately predict and engineer anisotropy for different electronic and spintronic applications.

To further probe the effect of thickness on the electrical transport, we performed Hall effect measurements for the IrO_2 (110) films. Figure 3a shows the Hall conductance at 1.8 K for different film thicknesses, as defined in eq 5 of the Supporting

https://doi.org/10.1021/acs.nanolett.4c02367
Nano Lett. 2024, 24, 10850−10857

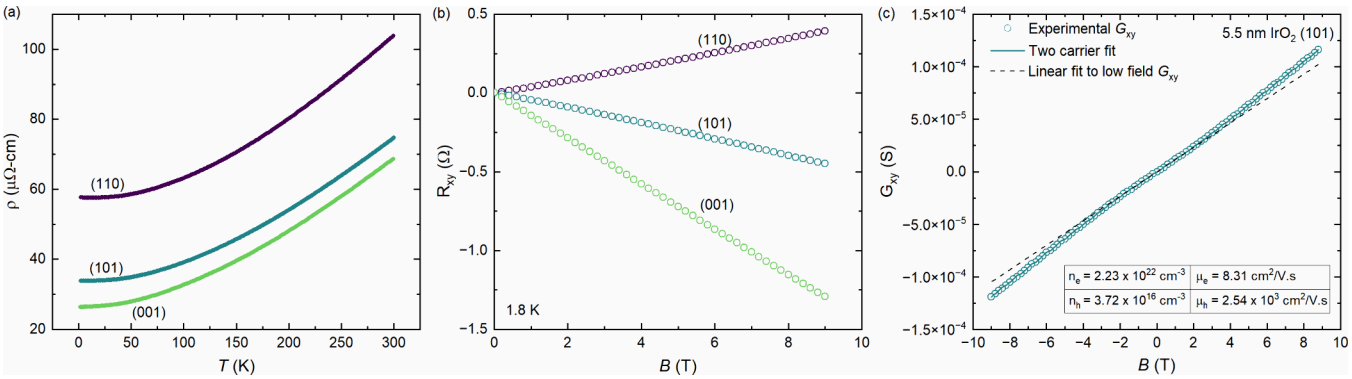

Figure 4. (a) Resistivity as a function of temperature for IrO_2 films of nominally same thickness (~5.5−5.8 nm) grown along different out-of-plane orientations on corresponding TiO_2 substrates. (b) Hall resistance as a function of magnetic field at 1.8 K for IrO_2 films shown in (a). (c) Hall conductance as a function of magnetic field for a IrO_2 (101) film along with two-carrier model fit used to extract the carrier concentrations and mobilities of the two channels shown in the inset table. A straight line fit to the low magnetic field (−0.4 to 0.4 T) Hall conductance is also plotted for better visualization of the nonlinear Hall effect.

Information, plotted against the applied magnetic field. We observed dominant hole carriers with an increasing concentration (increasing slope) as a function of film thickness. A closer look at the Hall conductance revealed a sizable nonlinearity for the low film thicknesses as shown in the inset of Figure 3a (Hall conductance for the 5.5 nm film). The thickness dependence of the nonlinear Hall effect (which suggests a possible role of strain relaxation) can be better visualized using the first-order derivative of Hall conductance plotted as a function of applied magnetic field. As shown in Figure S2a, a peak is observed in the derivative plot near zero magnetic field, a feature that vanishes with increasing film thickness. The nonlinearity can also be estimated using the difference between the experimental data and linear fits to the low-field region as shown in Figure S2b. The separation between the experimental data and linear fit can be observed to decrease with an increasing film thickness. This is quantitatively captured in Figure S2c, where the percentage difference between the linear fit and the experimental Hall conductance at 9 T is plotted as a function of film thickness. An exponential-like decay was observed for this parameter with increasing thickness. The nonlinear Hall effect was further analyzed using a two-carrier model (eq 2) as proposed by Bansal et al.[51] and described in the Supporting Information. A two-carrier conduction model is justified due to the presence of both electron and hole pockets on the Fermi surface of IrO_2.

$$G_{xy}(B) = eB\left(\frac{c_1\mu_2 - c_2}{(\mu_2/\mu_1 - 1)(1 + \mu_1^2 B^2)} + \frac{c_1\mu_1 - c_2}{(\mu_2/\mu_1 - 1)(1 + \mu_2^2 B^2)}\right) \quad (2)$$

As shown in the inset of Figure 3a, excellent fits were obtained by using eq 2 with c_1 and c_2 as the fit parameters. c_1 and c_2 are functions of the carrier concentrations and mobilities of the two conduction channels. Strikingly, the two-carrier analysis revealed the presence of high-mobility minority electron carriers along with low-mobility majority hole carriers. As shown in Figure 3b,c, the minority electron concentration varied between 10^{15} and 10^{17} cm^{-3} and their mobilities exceeded 3000 $cm^2/(V\,s)$. This extracted high mobility is quite remarkable given the traditionally low electron mobilities in most oxide materials.

Although a nonlinear Hall effect has not been observed before in IrO_2, the presence of the different carrier types has been experimentally demonstrated[34] before using Hall effect measurements on IrO_2 films with different epitaxial orientations. Since the Fermi surface of IrO_2 includes both electron and hole pockets,[24,25] it is plausible that Hall measurements will show both electrons and holes as majority and/or minority carriers depending on the crystal orientation. To confirm this effect for the IrO_2 (110) films used in this study, we also studied epitaxial IrO_2 (101) and IrO_2 (001) films on the corresponding TiO_2 substrates. As shown in Figure 4a, we observed that for similar film thicknesses the (110)-oriented films showed considerably higher resistivity as compared to the other orientations. This observation deviates from previous reports[24,34] where the (110)-oriented films were found to have either similar or lower resistivity. The origin of this discrepancy is currently not understood. Differences in the exact strain states, dislocations, and point defects can be possible factors. Nonetheless, the Hall effect measurements shown in Figure 4b revealed varying dominant carrier type, in agreement with ref 34, where Hall coefficient calculations using a nonsymmorphic tight binding model were used to explain the observed magnetic-field-direction-dependent majority carriers. We observed dominant hole conduction in the (110)-oriented film and dominant electron conduction in the (101)- and (001)-oriented films. Remarkably, we also observed strong nonlinearity in the Hall conductance for the (101)-oriented sample as shown in Figure 4c. Unlike IrO_2 (110), the IrO_2 (101) film showed low-mobility majority electron carriers (n_e = 2.23 × 10^{22} cm^{-3}; μ_e = 8.31 $cm^2/(V\,s)$) and high-mobility minority hole carriers (n_h = 3.72 × 10^{16} cm^{-3}; μ_h = 2540 $cm^2/(V\,s)$) as extracted from the two-carrier model. The observation of both high-mobility electron and hole carriers as a function of film orientation (which also governs epitaxial strain and current direction) in IrO_2 raises questions about their origin and necessitates further investigation. In addition, we also observed weak nonlinearity starting to appear at magnetic fields higher than 6−7 T for the IrO_2 (001) film, which needs to be further verified with Hall measurements at magnetic fields higher than 9 T.

To summarize, we have studied the electrical transport properties in IrO_2 films using a combination of temperature-dependent DC resistivity measurements and low-temperature Hall resistance measurements. The analysis of the temperature-

https://doi.org/10.1021/acs.nanolett.4c02367
Nano Lett. 2024, 24, 10850−10857

dependent resistivity measurements for epitaxial IrO_2 (110) films with different thicknesses showed that interband acoustic and optical phonon scatterings are the dominant scattering mechanisms in normal state transport. The extracted electron−phonon coupling constants agree well with previously reported values in the literature, and the extracted Debye temperature of 430 K agrees well with the approach to *T*-linear behavior observed around 400 K. The measured IrO_2 (110) samples also showed a thickness-dependent in-plane resistance anisotropy which is likely a result of strain-relaxation-induced changes in orbital hybridization and Fermi level density of states. The effect of thickness and epitaxial strain was also observed in the emergent nonlinearity in the Hall resistance, and a two-carrier model analysis of the nonlinearity revealed the presence of high-mobility minority carriers. The observation of multiple carrier types was also confirmed using IrO_2 films with different epitaxial orientations, which showed varying carrier properties in terms of charge, concentration, and mobilities, attesting to the complex Fermi surface and potential origins of these unusual transport features in the topological nature of the electronic band structure of IrO_2.

■ ASSOCIATED CONTENT

Data Availability Statement

All relevant data are included in the main text and Supporting Information. Any additional information can be requested from the corresponding authors.

Supporting Information

The Supporting Information is available free of charge at https://pubs.acs.org/doi/10.1021/acs.nanolett.4c02367.

Experimental methods and details of scattering terms included in eq 1, extracted fit parameters for eq 1, additional analysis of resistivity, and Hall conductance along with a description of the two-carrier model used to fit Hall conductance data (PDF)

■ AUTHOR INFORMATION

Corresponding Authors

Sreejith Nair − *Department of Chemical Engineering and Materials Science, University of Minnesota, Twin Cities, Minneapolis, Minnesota 55455, United States;* orcid.org/0000-0002-4457-2698; Email: nair0074@umn.edu

Bharat Jalan − *Department of Chemical Engineering and Materials Science, University of Minnesota, Twin Cities, Minneapolis, Minnesota 55455, United States;* orcid.org/0000-0002-7940-0490; Email: bjalan@umn.edu

Authors

Zhifei Yang − *Department of Chemical Engineering and Materials Science, University of Minnesota, Twin Cities, Minneapolis, Minnesota 55455, United States; School of Physics and Astronomy, University of Minnesota, Twin Cities, Minneapolis, Minnesota 55455, United States*

Kevin Storr − *Department of Physics, Prairie View A&M University, Prairie View, Texas 77446-0519, United States*

Complete contact information is available at: https://pubs.acs.org/10.1021/acs.nanolett.4c02367

Author Contributions

S.N. and B.J. designed the experiments. S.N. grew the IrO_2 films. S.N. and Z.Y. performed electrical and magnetotransport measurements and data analysis. S.N. and K.S. discussed the transport data. S.N. and B.J. wrote the manuscript. B.J. supervised all aspects of the project. All authors contributed to the discussion of the manuscript.

Notes

The authors declare no competing financial interest.

■ ACKNOWLEDGMENTS

This work was supported primarily by the Air Force Office of Scientific Research (AFOSR) through Grant Nos. FA9550-21-1-0025 and FA9550-23-1-0247. K.S. acknowledges support from the AFOSR through Grant Nos. FA9550-22-1-0205 and FA9550-24-1-004. Film growth was performed using instrumentation funded by AFOSR DURIP awards FA9550-18-1-0294 and FA9550-23-1-0085. Film growth (S.N.) was supported by the U.S. Department of Energy through award No. DE-SC0024710. Z.Y. received partial support from the UMN MRSEC program under Award No. DMR-2011401. Parts of this work were carried out at the Characterization Facility, University of Minnesota, which receives partial support from the NSF through the MRSEC program under award DMR-2011401. Device fabrication was carried out at the Minnesota Nano Center, which is supported by the NSF through the National Nano Coordinated Infrastructure under award ECCS-2025124.

■ REFERENCES

(1) Zylbersztejn, A.; Mott, N. F. Metal-insulator transition in vanadium dioxide. *Phys. Rev. B* **1975**, *11* (11), 4383−4395.

(2) Aetukuri, N. B.; Gray, A. X.; Drouard, M.; Cossale, M.; Gao, L.; Reid, A. H.; Kukreja, R.; Ohldag, H.; Jenkins, C. A.; Arenholz, E.; Roche, K. P.; Dürr, H. A.; Samant, M. G.; Parkin, S. S. P. Control of the metal-insulator transition in vanadium dioxide by modifying orbital occupancy. *Nat. Phys.* **2013**, *9* (10), 661−666.

(3) Taha, M.; Walia, S.; Ahmed, T.; Headland, D.; Withayachumnankul, W.; Sriram, S.; Bhaskaran, M. Insulator-metal transition in substrate-independent VO_2 thin film for phase-change devices. *Sci. Rep.* **2017**, *7* (1), 17899.

(4) Martens, K.; Jeong, J. W.; Aetukuri, N.; Rettner, C.; Shukla, N.; Freeman, E.; Esfahani, D. N.; Peeters, F. M.; Topuria, T.; Rice, P. M.; Volodin, A.; Douhard, B.; Vandervorst, W.; Samant, M. G.; Datta, S.; Parkin, S. S. P. Field Effect and Strongly Localized Carriers in the Metal-Insulator Transition Material VO_2. *Phys. Rev. Lett.* **2015**, *115* (19), 196401.

(5) Schofield, P.; Bradicich, A.; Gurrola, R. M.; Zhang, Y.; Brown, T. D.; Pharr, M.; Shamberger, P. J.; Banerjee, S. Harnessing the Metal-Insulator Transition of VO_2 in Neuromorphic Computing. *Adv. Mater.* **2023**, *35* (37), 2205294.

(6) Ruf, J. P.; Paik, H.; Schreiber, N. J.; Nair, H. P.; Miao, L.; Kawasaki, J. K.; Nelson, J. N.; Faeth, B. D.; Lee, Y.; Goodge, B. H.; Pamuk, B.; Fennie, C. J.; Kourkoutis, L. F.; Schlom, D. G.; Shen, K. M. Strain-stabilized superconductivity. *Nat. Commun.* **2021**, *12* (1), 59.

(7) Jovic, V.; Koch, R. J.; Panda, S. K.; Berger, H.; Bugnon, P.; Magrez, A.; Smith, K. E.; Biermann, S.; Jozwiak, C.; Bostwick, A.; Rotenberg, E.; Moser, S. Dirac nodal lines and flat-band surface state in the functional oxide RuO_2. *Phys. Rev. B* **2018**, *98* (24), 241101.

(8) Feng, Z.; Zhou, X.; Šmejkal, L.; Wu, L.; Zhu, Z.; Guo, H.; González-Hernández, R.; Wang, X.; Yan, H.; Qin, P.; Zhang, X.; Wu, H.; Chen, H.; Meng, Z.; Liu, L.; Xia, Z.; Sinova, J.; Jungwirth, T.; Liu, Z. An anomalous Hall effect in altermagnetic ruthenium dioxide. *Nature Electronics* **2022**, *5* (11), 735−743.

(9) Šmejkal, L.; Sinova, J.; Jungwirth, T. Emerging Research Landscape of Altermagnetism. *Physical Review X* **2022**, *12* (4), 040501.

(10) Berlijn, T.; Snijders, P. C.; Delaire, O.; Zhou, H. D.; Maier, T. A.; Cao, H. B.; Chi, S. X.; Matsuda, M.; Wang, Y.; Koehler, M. R.;

Kent, P. R. C.; Weitering, H. H. Itinerant Antiferromagnetism in RuO_2. *Phys. Rev. Lett.* **2017**, *118* (7), 077201.
(11) Gyo Jeong, S.; Choi, I. H.; Nair, S.; Buiarelli, L.; Pourbahari, B.; Oh, J. Y.; Bassim, N.; Seo, A.; Choi, W. S.; Fernandes, R. M.; Birol, T.; Zhao, L.; Lee, J. S.; Jalan, B. Altermagnetic Polar Metallic phase in Ultra-Thin Epitaxially-Strained RuO_2 Films. *arXiv (Condensed Matter: Materials Science)*, 2024-05-09. DOI: 10.48550/arXiv.2405.05838 (accessed 2024-08-08).
(12) Bose, A.; Schreiber, N. J.; Jain, R.; Shao, D.-F.; Nair, H. P.; Sun, J.; Zhang, X. S.; Muller, D. A.; Tsymbal, E. Y.; Schlom, D. G.; Ralph, D. C. Author Correction: Tilted spin current generated by the collinear antiferromagnet ruthenium dioxide. *Nature Electronics* **2022**, *5* (10), 706−706.
(13) Jiang, Y.-Y.; Wang, Z.-A.; Samanta, K.; Zhang, S.-H.; Xiao, R.-C.; Lu, W. J.; Sun, Y. P.; Tsymbal, E. Y.; Shao, D.-F. Prediction of giant tunneling magnetoresistance in $RuO_2/TiO_2/RuO_2$ (110) antiferromagnetic tunnel junctions. *Phys. Rev. B* **2023**, *108* (17), 174439.
(14) Shao, D.-F.; Zhang, S.-H.; Li, M.; Eom, C.-B.; Tsymbal, E. Y. Spin-neutral currents for spintronics. *Nat. Commun.* **2021**, *12* (1), 7061.
(15) Zhang, T. X.; Coughlin, A. L.; Lu, C.-K.; Heremans, J. J.; Zhang, S. X. Recent progress on topological semimetal IrO_2: electronic structures, synthesis, and transport properties. *J. Phys.: Condens. Matter* **2024**, *36* (27), 273001.
(16) Pesin, D.; Balents, L. Mott physics and band topology in materials with strong spin-orbit interaction. *Nat. Phys.* **2010**, *6* (5), 376−381.
(17) Laurell, P.; Fiete, G. A. Topological Magnon Bands and Unconventional Superconductivity in Pyrochlore Iridate Thin Films. *Phys. Rev. Lett.* **2017**, *118* (17), 177201.
(18) Savary, L.; Moon, E.-G.; Balents, L. New Type of Quantum Criticality in the Pyrochlore Iridates. *Physical Review X* **2014**, *4* (4), 041027.
(19) Wang, F.; Senthil, T. Twisted Hubbard Model for Sr_2IrO_4: Magnetism and Possible High Temperature Superconductivity. *Phys. Rev. Lett.* **2011**, *106* (13), 136402.
(20) Chen, Y.; Lu, Y.-M.; Kee, H.-Y. Topological crystalline metal in orthorhombic perovskite iridates. *Nat. Commun.* **2015**, *6* (1), 6593.
(21) Liu, Z. T.; Li, M. Y.; Li, Q. F.; Liu, J. S.; Li, W.; Yang, H. F.; Yao, Q.; Fan, C. C.; Wan, X. G.; Wang, Z.; Shen, D. W. Direct observation of the Dirac nodes lifting in semimetallic perovskite $SrIrO_3$ thin films. *Sci. Rep.* **2016**, *6* (1), 30309.
(22) Nan, T.; Anderson, T. J.; Gibbons, J.; Hwang, K.; Campbell, N.; Zhou, H.; Dong, Y. Q.; Kim, G. Y.; Shao, D. F.; Paudel, T. R.; Reynolds, N.; Wang, X. J.; Sun, N. X.; Tsymbal, E. Y.; Choi, S. Y.; Rzchowski, M. S.; Kim, Y. B.; Ralph, D. C.; Eom, C. B. Anisotropic spin-orbit torque generation in epitaxial $SrIrO_3$ by symmetry design. *Proc. Natl. Acad. Sci. U. S. A.* **2019**, *116* (33), 16186−16191.
(23) Sun, Y.; Zhang, Y.; Liu, C.-X.; Felser, C.; Yan, B. Dirac nodal lines and induced spin Hall effect in metallic rutile oxides. *Phys. Rev. B* **2017**, *95* (23), 235104.
(24) Nelson, J. N.; Ruf, J. P.; Lee, Y.; Zeledon, C.; Kawasaki, J. K.; Moser, S.; Jozwiak, C.; Rotenberg, E.; Bostwick, A.; Schlom, D. G.; Shen, K. M.; Moreschini, L. Dirac nodal lines protected against spin-orbit interaction in IrO_2. *Physical Review Materials* **2019**, *3* (6), 064205.
(25) Xu, X.; Jiang, J.; Shi, W. J.; Süß, V.; Shekhar, C.; Sun, S. C.; Chen, Y. J.; Mo, S. K.; Felser, C.; Yan, B. H.; Yang, H. F.; Liu, Z. K.; Sun, Y.; Yang, L. X.; Chen, Y. L. Strong spin-orbit coupling and Dirac nodal lines in the three-dimensional electronic structure of metallic rutile IrO_2. *Phys. Rev. B* **2019**, *99* (19), 195106.
(26) Das, P. K.; Sławińska, J.; Vobornik, I.; Fujii, J.; Regoutz, A.; Kahk, J. M.; Scanlon, D. O.; Morgan, B. J.; McGuinness, C.; Plekhanov, E.; Di Sante, D.; Huang, Y.-S.; Chen, R.-S.; Rossi, G.; Picozzi, S.; Branford, W. R.; Panaccione, G.; Payne, D. J. Role of spin-orbit coupling in the electronic structure of IrO_2. *Physical Review Materials* **2018**, *2* (6), 065001.
(27) Bose, A.; Nelson, J. N.; Zhang, X. S.; Jadaun, P.; Jain, R.; Schlom, D. G.; Ralph, D. C.; Muller, D. A.; Shen, K. M.; Buhrman, R. A. Effects of Anisotropic Strain on Spin-Orbit Torque Produced by the Dirac Nodal Line Semimetal IrO_2. *ACS Appl. Mater. Interfaces* **2020**, *12* (49), 55411−55416.
(28) Patton, M.; Gurung, G.; Shao, D.-F.; Noh, G.; Mittelstaedt, J. A.; Mazur, M.; Kim, J.-W.; Ryan, P. J.; Tsymbal, E. Y.; Choi, S.-Y.; Ralph, D. C.; Rzchowski, M. S.; Nan, T.; Eom, C.-B. Symmetry Control of Unconventional Spin-Orbit Torques in IrO_2. *Adv. Mater.* **2023**, *35* (39), 2301608.
(29) Kahk, J. M.; Poll, C. G.; Oropeza, F. E.; Ablett, J. M.; Céolin, D.; Rueff, J. P.; Agrestini, S.; Utsumi, Y.; Tsuei, K. D.; Liao, Y. F.; Borgatti, F.; Panaccione, G.; Regoutz, A.; Egdell, R. G.; Morgan, B. J.; Scanlon, D. O.; Payne, D. J. Understanding the Electronic Structure of IrO_2 Using Hard-X-ray Photoelectron Spectroscopy and Density-Functional Theory. *Phys. Rev. Lett.* **2014**, *112* (11), 117601.
(30) Kim, W. J.; Kim, S. Y.; Kim, C. H.; Sohn, C. H.; Korneta, O. B.; Chae, S. C.; Noh, T. W. Spin-orbit coupling induced band structure change and orbital character of epitaxial IrO_2 films. *Phys. Rev. B* **2016**, *93* (4), 045104.
(31) Panda, S. K.; Bhowal, S.; Delin, A.; Eriksson, O.; Dasgupta, I. Effect of spin orbit coupling and Hubbard U on the electronic structure of IrO_2. *Phys. Rev. B* **2014**, *89* (15), 155102.
(32) Arias-Egido, E.; Laguna-Marco, M. A.; Piquer, C.; Jiménez-Cavero, P.; Lucas, I.; Morellón, L.; Gallego, F.; Rivera-Calzada, A.; Cabero-Piris, M.; Santamaria, J.; Fabbris, G.; Haskel, D.; Boada, R.; Díaz-Moreno, S. Dimensionality-driven metal-insulator transition in spin-orbit-coupled IrO_2. *Nanoscale* **2021**, *13* (40), 17125−17135.
(33) Kawasaki, J. K.; Kim, C. H.; Nelson, J. N.; Crisp, S.; Zollner, C. J.; Biegenwald, E.; Heron, J. T.; Fennie, C. J.; Schlom, D. G.; Shen, K. M. Engineering Carrier Effective Masses in Ultrathin Quantum Wells of IrO_2. *Phys. Rev. Lett.* **2018**, *121* (17), 176802.
(34) Uchida, M.; Sano, W.; Takahashi, K. S.; Koretsune, T.; Kozuka, Y.; Arita, R.; Tokura, Y.; Kawasaki, M. Field-direction control of the type of charge carriers in nonsymmorphic IrO_2. *Phys. Rev. B* **2015**, *91* (24), 241119.
(35) Goodenough, J. B. Direct Cation- -Cation Interactions in Several Oxides. *Phys. Rev.* **1960**, *117* (6), 1442−1451.
(36) Goodenough, J. B. Metallic oxides. *Prog. Solid State Chem.* **1971**, *5*, 145−399.
(37) Occhialini, C. A.; Bisogni, V.; You, H.; Barbour, A.; Jarrige, I.; Mitchell, J. F.; Comin, R.; Pelliciari, J. Local electronic structure of rutile RuO_2. *Physical Review Research* **2021**, *3* (3), 033214.
(38) Ryden, W. D.; Lawson, A. W.; Sartain, C. C. Temperature dependence of the resistivity of RuO_2 and IrO_2. *Phys. Lett. A* **1968**, *26* (5), 209−210.
(39) Nunn, W.; Manjeshwar, A. K.; Yue, J.; Rajapitamahuni, A.; Truttmann, T. K.; Jalan, B. Novel synthesis approach for "stubborn" metals and metal oxides. *Proc. Natl. Acad. Sci. U. S. A.* **2021**, *118* (32), No. e2105713118.
(40) Nunn, W.; Nair, S.; Yun, H.; Manjeshwar, A. K.; Rajapitamahuni, A.; Lee, D.; Mkhoyan, K. A.; Jalan, B. Solid source metal-organic molecular beam epitaxy of epitaxial RuO_2. *APL Mater.* **2021**, *9*, 091112.
(41) Nair, S.; Yang, Z.; Lee, D.; Guo, S.; Sadowski, J. T.; Johnson, S.; Saboor, A.; Li, Y.; Zhou, H.; Comes, R. B.; Jin, W.; Mkhoyan, K. A.; Janotti, A.; Jalan, B. Engineering metal oxidation using epitaxial strain. *Nat. Nanotechnol.* **2023**, *18* (9), 1005−1011.
(42) Liao, Z.; Li, F.; Gao, P.; Li, L.; Guo, J.; Pan, X.; Jin, R.; Plummer, E. W.; Zhang, J. Origin of the metal-insulator transition in ultrathin films of $La_{2/3}Sr_{1/3}MnO_3$. *Phys. Rev. B* **2015**, *92* (12), 125123.
(43) Wang, G.; Wang, Z.; Meng, M.; Saghayezhian, M.; Chen, L.; Chen, C.; Guo, H.; Zhu, Y.; Plummer, E. W.; Zhang, J. Role of disorder and correlations in the metal-insulator transition in ultrathin $SrVO_3$ films. *Phys. Rev. B* **2019**, *100* (15), 155114.
(44) Rajapitamahuni, A. K.; Nair, S.; Yang, Z.; Kamath Manjeshwar, A.; Gyo Jeong, S.; Nunn, W.; Jalan, B. Thickness-dependent insulator-to-metal transition in epitaxial RuO_2 films. *Physical Review Materials* **2024**, *8* (7), 075002.

https://doi.org/10.1021/acs.nanolett.4c02367
Nano Lett. 2024, 24, 10850−10857

(45) Lin, J. J.; Huang, S. M.; Lin, Y. H.; Lee, T. C.; Liu, H.; Zhang, X. X.; Chen, R. S.; Huang, Y. S. Low temperature electrical transport properties of RuO_2 and IrO_2 single crystals. *J. Phys.: Condens. Matter* **2004**, *16* (45), 8035.
(46) Lin, Y. H.; Sun, Y. C.; Jian, W. B.; Chang, H. M.; Huang, Y. S.; Lin, J. J. Electrical transport studies of individual IrO_2 nanorods and their nanorod contacts. *Nanotechnology* **2008**, *19* (4), 045711.
(47) Glassford, K. M.; Chelikowsky, J. R. Electronic and structural properties of RuO_2. *Phys. Rev. B* **1993**, *47* (4), 1732−1741.
(48) Korotcov, A. V.; Huang, Y.-S.; Tiong, K.-K.; Tsai, D.-S. Raman scattering characterization of well-aligned RuO_2 and IrO_2 nanocrystals. *J. Raman Spectrosc.* **2007**, *38* (6), 737−749.
(49) Liao, P. C.; Chen, C. S.; Ho, W. S.; Huang, Y. S.; Tiong, K. K. Characterization of IrO_2 thin films by Raman spectroscopy. *Thin Solid Films* **1997**, *301* (1), 7−11.
(50) Price, W. L. V. Extension of van der Pauw's theorem for measuring specific resistivity in discs of arbitrary shape to anisotropic media. *J. Phys. D: Appl. Phys.* **1972**, *5* (6), 1127.
(51) Bansal, N.; Kim, Y. S.; Brahlek, M.; Edrey, E.; Oh, S. Thickness-Independent Transport Channels in Topological Insulator Bi_2Se_3 Thin Films. *Phys. Rev. Lett.* **2012**, *109* (11), 116804.
(52) Bongers, P. F. Anisotropy of the electrical conductivity of VO_2 single crystals. *Solid State Commun.* **1965**, *3* (9), 275−277.
(53) Rodbell, D. S.; Lommel, J. M.; Devries, R. C. Electrical Resistivity of Single Crystal CrO_2. *J. Phys. Soc. Jpn.* **1966**, *21* (11), 2430−2430.

https://doi.org/10.1021/acs.nanolett.4c02367
Nano Lett. 2024, 24, 10850−10857